Long-term polarimetric observations of OH127.8+0.0

P. Wolak[1]*, M. Szymczak[1] and E. Gérard[2]

[1] *Toruń Centre for Astronomy, Nicolaus Copernicus University, Gagarina 11, 87-100 Toruń, Poland*
[2] *GEPI, UMR 8111, Observatoire de Paris, 5 place J. Janssen, 92195 Meudon Cedex, France*

ABSTRACT
OH 1612- and 1667-MHz masers from the well known object OH127.8+0.0 were monitored in full-polarization mode over a period of 6.5 years and mapped with MERLIN at one epoch. The OH variability pattern of the star is typical of extremely long-period AGB stars. The distance determined from the 1612-MHz light curve and a new measurement of the angular radius is 3.87 ± 0.28 kpc. At both frequencies, the flux of polarized emission tightly follows the total flux variations while, the degrees of circular and linear polarization are constant within measurement accuracy.. There is net polarization at both lines. The magnetic field strength estimated from a likely Zeeman pair is -0.6 mG at the distance of 5400 au from the star. At the near and far sides of the envelope, the polarization vectors are well aligned implying a regular structure of the magnetic field. The polarization characteristics of the OH maser emission suggest a radial magnetic field which is frozen in the stellar wind.

Key words: masers – polarization – circumstellar matter – stars: AGB and post-AGB

1 INTRODUCTION

OH/IR stars have a spectral energy distribution which peaks between 10 and 25μm, an absorption feature at 9.7μm and a double-peaked OH maser profile at 1612 MHz. Almost all of them are long period variables with periods of 500–3000 days and bolometric amplitudes of 1–2 magnitudes (Habing 1996). As low and intermediate mass stars with enhanced mass loss up to a few $10^{-5} M_\odot$ yr^{-1}, which leads to a very optically thick and dusty circumstellar envelope, they could be considered as successors of Miras (van der Veen & Habing 1988; Vassiliadis & Wood 1993; Habing 1996). Untargeted surveys of OH 1612-MHz line suggested that OH/IR stars have progenitor masses from 1 to $8 M_\odot$ (Baud et al. 1981). OH/IR objects with periods above 1000 days are thought to be probably medium mass ($\geqslant 4.5 M_\odot$) evolved objects (Likkel 1989; Lépine, Ortiz & Epchtein 1995; Habing 1996). The study of mid-infrared spectral features in a large sample of circumstellar OH masers provides indirect evidence for mass segregation between Miras and OH/IR objects (Chen et al. 2001). One of the ways to verify this hypothesis and to constrain the evolutionary status of OH/IR stars is to assess their parameters using reliable distances.

OH127.8+0.0 (= OH127 = IRAS01304+6211 = V669 Cas) was discovered in a small-scale untargeted survey at 1612 MHz (Kerr & Bowers 1974). High angular resolution studies of this brightest OH/IR star in the anti-centre region

revealed a thin OH 1612-MHz maser shell of $\sim 1''.5$ radius expanding with a velocity of about 12 km s^{-1} (Booth et al. 1981; Norris, Diamond & Booth 1982; Bowers, Johnston & Spencer 1983). These observational characteristics are fully consistent with the predictions of the standard expanding shell model (Goldreich & Scoville 1976; Elitzur, Goldreich & Scoville 1976), although a large portion of the envelope shows departure from spherical symmetry. In this model, a thin spherical shell and double-peaked OH 1612-MHz profiles are the natural consequence of radial amplification of OH maser emission in a uniform outflow at a constant velocity (Reid et al. 1977). The star has received much attention over the years as an archetypal OH/IR object but its distance is poorly determined spreading from 2.9 to 6.2 kpc (van Langevelde, van der Heiden & van Schooneveld 1990; Bowers & Johnston 1990). In this paper we estimate its distance comparing the linear diameter of the shell, determined using the phase lag technique (Herman & Habing 1985), with the angular diameter measured on interferometric maps.

In early observations, the OH maser emission from OH/IR stars appeared largely unpolarized (Cohen 1989). However, our recent study has revealed polarized features in about 60% (33/57) of the OH/IR stars (Wolak, Szymczak & Gérard 2012). Elliptically polarized emission with a degree of polarization up to 30% is usually detected. This indicates the presence of magnetic fields in the outer envelopes. High angular resolution observations have revealed a magnetic field of a few mG, whose structure was imaged in several

* E-mail: wolak@astro.uni.torun.pl

late-type stars (Chapman & Cohen 1986; Szymczak, Cohen & Richards 1998, 2001; Bains et al. 2003; Amiri, Vlemmings & van Langevelde 2010). OH127 has been mapped several times with the VLA (Bowers et al. 1983; Bowers & Johnston 1990) and MERLIN (Booth et al. 1981; Norris et al. 1982) but no full polarization data were obtained. We present polarimetric maps of the target and analyze full polarization time series in order to explore the behaviour of the magnetic field and the degree of saturation of maser amplification.

2 OBSERVATIONS

2.1 Nançay

Data were obtained at 189 epochs during the period 2002 May 12 − 2008 December 28 (Table 1) with the Nançay radio telescope (NRT). A cooled $1.1-1.8$ GHz receiver and a 8192-channel autocorrelation spectrometer were used for simultaneous observations of the two OH transitions at 1612.231 and 1667.359 MHz. The receiver system temperature was about 35 K and the effective velocity resolution was 0.142 and 0.137 km s^{-1} at 1612 and 1667 MHz, respectively. The half-power beam width was $3.'5$(RA) by $19'$(Dec) and the conversion factor of the antenna temperature to the flux density for a point source was $\sim$1.4 K Jy^{-1}.

The two orthogonal linear polarizations and two opposite circular polarizations for each transitionwere measured in the 8-bank mode of the spectrometer. The Stokes parameters I, Q and V were directly provided by the system, while the Stokes U was extracted by a horn rotation of 45°. The four Stokes parameters were used to derive: the linearly polarized flux density, $p = \sqrt{Q^2 + U^2}$, degree of circular polarization, the $m_C = V/I$, degree of linear polarization, $m_L = p/I$ and the polarization position angle, $\chi = 0.5\tan^{-1}(U/Q)$. The absolute and relative accuracies of gain measured with a noise diode were $\sim$5% and $\sim$1%, respectively. The error in the polarized intensity caused by the polarization leakage between the orthogonal feeds was about 2%. The baseline subtraction was done by frequency switching: this mode introduces an error of less than 0.6% in the polarization parameters, as compared to the position switching mode. W12 (an unpolarized source in absorption) and W3OH (a strongly polarized maser source) were regularly observed throughout the whole project in order to measure the instrumental polarization and consistency of the amplitude calibration. The absolute flux density scale was accurate to within $7-8$%. A detailed description of the methods of observations, full polarization calibrations, analysis of errors is given in Szymczak & Gérard (2004). A total integration time for the two horn positions of $\sim$12 min resulted in a $3\sigma_{\rm rms}$ sensitivity level in the Stokes I of $\sim$0.4 Jy. All the velocities given in this paper are relative to the local standard of rest.

Since the upgrade of the NRT in 2001 (van Driel, Pezzani & Gérard 1996) interferences from local and/or satellite transmitters were reduced dramatically. Throughout the whole observing period, we noticed them at a few epochs only and the total loss of data was less than one per cent.

2.2 MERLIN

OH127 was observed in the 1612- and 1667-MHz OH transitions on 2001 December 21 using the six telescopes of the MERLIN array in full-polarization mode. The narrow-band (0.25 MHz) observations of the target switched at intervals of 3 minutes between the two maser lines and were interleaved with 1.5-min scans on 0141+579, the phase reference source, in wide-band mode (14 MHz) at the appropriate frequencies to obtain the optimum signal-to-noise ratio. The source 3C84 was observed both in narrow-band and wideband modes in order to determine the phase offset correction that arises due to observations made in different frequency setups and to derive corrections for instrumental gain variations across the bandpass. The flux density scale and the absolute polarization position angles were determined by observations of 3C286.

The data reduction was carried out following standard procedures for MERLIN OH polarimetry (Diamond et al. 2003) using the d-programs at Jodrell Bank and the Astronomical Image Processing System (AIPS). The I, Q, U and V data cubes were obtained with a beam of $0.''17 \times 0.''15$. The spectral channel width was 0.5 kHz, which corresponds to 0.10 and 0.09 km s^{-1} at 1612 and 1667 MHz respectively. The $1\sigma_{\rm rms}$ noise level in emission-free Stokes I single channel map was typically 17 mJy beam^{-1}. The error on the absolute flux scale is 5 per cent. The errors on the polarization angle were usually lower than $\pm 2.°0$ for the strongly polarized components. The absolute maser position error was ± 20 mas.

3 RESULTS

3.1 Total flux density curves

The variations of the total integrated flux densities at 1612 and 1667 MHz are shown in Figure 1. In order to represent the light curve shape a sum of two periodic functions of the type discussed by David, Etoka & Le Squeren (1996) was fitted to the data. The time of maximum for the red-shifted integrated flux density, T_0, the period, P, the amplitude measured in the logarithmic scale, Δm, and the asymmetry defined as the fraction of the period between minimum and maximum are given in Table 1. There are no significant differences in those parameters between the 1612 and 1667-MHz lines with the exception of Δm, which differs by a factor of 1.7. The ratios of the integrated flux at the two lines range from 5.4 at minimum light to 9.9 at maximum. This implies a partial suppression of the 1667-MHz emission as the brightness increases due to a competitive gain effect (Gray & Field 1996).

The total flux density at the two frequencies shows smooth and regular variations with the exception of a bump on the rising branch of the light curve near MJD $=$ JD$-2450000 = 4450$. A similar event occurred near JD $= 2446800$ as might be deduced from the 1612-MHz curve shown by van Langevelde et al. (1990) (their Fig. 2). The asymmetry deduced from our data is higher than that reported previously (Herman & Habing 1985; van Langevelde et al. 1990). The period inferred from our data is shorter by 434 days than reported in Herman & Habing (1985). It is also shorter by 38 days than the value given in van Langevelde et al. (1990) but is well within their uncertain-
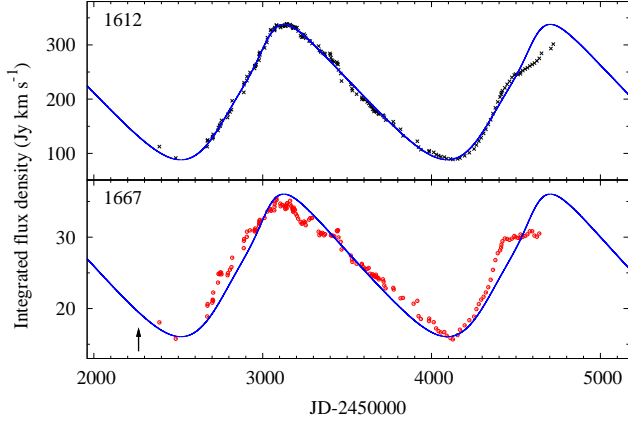
Figure 1. Integrated flux density of the OH 1612- (upper panel) and 1667-MHz (lower panel) spectra of OH127 as a function of time. The uncertainties of the measurements are comparable with the symbol sizes. The blue line shows the model light curve. The arrow marks the date of the MERLIN polarimetric observation.

Table 1. Measured and derived parameters for OH127.8+0.0.

Nançay data	
Span of monitoring data (MJD)	$2355 - 4735$
Number of observations	189
Expansion velocity, $V_e(1612)$ (km s^{-1})	11.13 ± 0.14
Expansion velocity, $V_e(1667)$ (km s^{-1})	11.31 ± 0.14
Stellar velocity, V_* (km s^{-1})	-54.78 ± 0.14
Time of maximum, $T_0(1612)$ (MJD)	3164.5 ± 2.5
Time of maximum, $T_0(1667)$ (MJD)	3086.1 ± 20.2
Period, $P(1612)$ (days)	1599.8 ± 4.1
Period, $P(1667)$ (days)	1596.1 ± 4.8
Amplitude, $\Delta m(1612)$ (mag)	1.416 ± 0.011
Amplitude, $\Delta m(1667)$ (mag)	0.829 ± 0.013
Asymmetry of the light curve (1612)	0.406 ± 0.006
Asymmetry of the light curve (1667)	0.343 ± 0.013
Phase lag, $\Delta\Phi(1612)$ (days)	61.81 ± 1.10
Shell radius (au)	5358.3 ± 95.7
MERLIN data	
RA offset of the shell centre[a] (mas)	0.0
Dec offset of the shell centre[a] (mas)	-191.0
Outer shell radius, $r_o(1612)$ (mas)	1380 ± 40
Inner shell radius, $r_i(1612)$ (mas)	1150 ± 40
Expansion velocity, $V_e(1612)$ (km s^{-1})	11.7 ± 0.2
Outer shell radius, $r_o(1667)$ (mas)	1340 ± 70
Inner shell radius, $r_i(1667)$ (mas)	1120 ± 70
Expansion velocity, $V_e(1667)$ (km s^{-1})	11.4 ± 0.2
Stellar velocity, V_* (km s^{-1})	-54.95 ± 0.20
Distance (kpc)	3.87 ± 0.28

[a]Relative to the phase centre of
RA(J2000) = $01^h 33^m 51^s.232$, Dec(J2000) = $62^0 26' 53''.236$

ties. An ephemeris of the time of maximum based on Herman & Habing and van Langevelde et al.'s data is inconsistent with that derived from our observations covering about one and half cycles. The large errors in their estimates cannot account for that inconsistency and we suggest significant changes of the light curve of OH127 from one cycle to the next. We conclude that the OH maser curves of OH127 strongly resemble the general characteristics of the optical light curve of long-period (<600 days) and extremely long-period (~1850 days) Miras (Lebzelter 2011; Groenewegen et al. 2009).

3.2 Phase lag

The time shifts between the 1612-MHz flux curves of individual channels, i.e. phase lags are determined using the following method. The light curves of each channel were normalized and smoothed with a three-point running mean and linearly interpolated to obtain uniformly one-day spaced data. The channel with the strongest emission at -65.9 km s^{-1} was chosen as a reference, i.e. as the zero point of the phase lag. All the other channels were scaled in amplitude and shifted in time to minimize the least squares difference between their light curves and that of the reference channel. The phase lags of all channels are plotted in Figure 2. The linear relation between the phase lag and velocity is fully consistent with the model of a uniformly expanding shell. The phase lag between the strongest blue- and red-shifted peaks, $\Delta\Phi$, is 61.81 ± 1.10 days (Table 1). Although the light curve is not strictly the same for each stellar cycle, the interpolation and smoothing applied to the data do not affect the phase lag because our observations were highly sampled with a typical time resolution of two weeks ($\sim 0.009P$).

Our value of $\Delta\Phi$ differs significantly from that of 75.6 ± 3.6 days and 41.4 ± 8.1 days reported by Herman & Habing (1985) and by van Langevelde et al. (1990), respectively. Such a drastic difference between these previous estimates of the phase lag is likely to be due to their different methods as, the two teams used a similar data sets. Our method is similar to that of van Langevelde et al., but the

data have a much higher temporal sampling. We confirm an asymmetry of the OH shell that may cause an error in the phase lag measurements of up to 15% (Bowers & Johnston 1990).

3.3 Polarization spectra and light curve

Figures 3 and 4 show the average polarization spectra near the maximum and minimum and the time series of polarization parameters for the strongest features at 1612 and 1667 MHz, respectively.

The expansion velocity defined as the half-maximum width in the OH profile peaks at 1612-MHz, $V_e(1612)$ does not differ from that at 1667-MHz, $V_e(1667)$ (Table 1). The stellar velocity determined as the mean velocity of the outer 1612-MHz peaks, V_* (Table 1) and the OH expansion velocities are quite consistent with previous estimates (Bowers & Johnston 1990). The outflow velocity of 13.0 km s^{-1} determined from the observations of CO transitions (De Beck et al. 2010) suggests that the OH masers form in regions which still did not reach the terminal velocity.

The 1612-MHz profile shows strong left hand circularly (LHC) polarized emission over almost the whole velocity range. The degree of circular polarization is usually lower than 20%. It generally decreases with an increase of the total flux density presumably due to depolarization effect. The degree of linear polarization is generally lower than 6% and
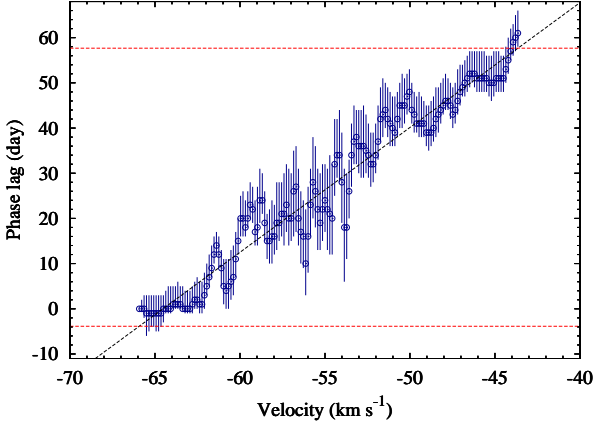
Figure 2. Phase lag between the light curves of spectral channels in the 1612-MHz spectrum of OH127 plotted against the velocity. The dashed black line is the best least squares fit to the whole data set. The red lines cross the best fit line at the velocities of the strongest blue- and red-shifted peaks.

Table 2. Mean and median values of the polarization parameters for the brightest OH features derived from the multi-epoch data.

Line (MHz)	Velocity (km s^{-1})	Parameter	Mean	SD[a]	Median
1612	−65.92	$m_C(\%)$	−5.34	1.81	−5.32
		$m_L(\%)$	5.13	1.90	5.00
		$\chi(°)$	−13.53	6.97	−25.02
	−43.65	$m_C(\%)$	−1.46	1.68	−1.41
		$m_L(\%)$	2.53	1.12	2.45
		$\chi(°)$	−23.32	13.14	−25.03
1667	−44.02	$m_C(\%)$	−7.20	2.18	−7.07
		$m_L(\%)$	6.05	1.56	5.81
		$\chi(°)$	12.95	12.86	11.82

[a] Standard deviation

shows a slight difference between the blue- and red-shifted parts of the spectrum. The polarization position angle is very similar in all spectral channels with a mean value of $-14.°7\pm1.°5$.

The 1667-MHz profile also shows strong LHC emission, but a relatively narrow polarized feature is seen only in the red-shifted part of the spectrum and m_C is lower than 12%. A linearly polarized feature is also detected in the red-shifted edge of the emission. The maximum value of m_L is 6–7%, while the χ angle changes rapidly across the profile of 1.1 km s^{-1} width, the mean value being $10.°2\pm7.°6$. We conclude that the quantitative polarization properties of the 1612- and 1667-MHz maser profiles of OH127 are typical for OH/IR objects in the sample recently studied (Wolak et al. 2012).

The timeseries of all polarization parameters of the brightest 1612- and 1667-MHz features at the blue- and red-shifted parts of the spectrum (Figs. 3 and 4) exhibit regular variations of the Stokes V and p fluxes tightly correlated with the total flux variations. The mean and median values of the degrees of circular and linear polarization and the polarization angle of those features are summarized in Table 2. The degrees of circular and linear polarization were constant within the uncertainty of instrumental polarization of about 2–3%. The polarization angle also does not show any systematic variations higher than 8–13°. Outliers in the plots are of instrumental origin, probably due to unbalanced gains of both types of polarization that we could not correct using the calibration data available. We found that the difference between the average polarization position angles for the four brightest blue- and red-shifted channels of the 1612-MHz profile was $1.°0\pm13.°5$. This suggests that the 1612-MHz maser regions are permeated with a regular magnetic field that is stable over a ∼6.5 year period. The linearly polarized emission at 1667 MHz was detected only in the red-shifted part of the profile. In the velocity range of −43.9 to −43.6 km s^{-1} the mean difference of χ between 1667- and 1612-MHz spectra is only $6.°5\pm15.°3$ but it increases to $46.°9\pm18.°4$ for the range −44.6 to −44.0 km s^{-1}. This indicates nearly the same projected direction of mag-

netic fields in the compact regions of the far sides of the 1612-MHz and 1667-MHz shells, whereas in the annular regions, these transitions likely probe different clouds.

3.4 Shell parameters and distance

The maps of OH emission at 1612 and 1667 MHz are well known (Booth et al. 1981; Norris et al. 1982; Bowers et al. 1983; Diamond et al. 1985; Bowers & Johnston 1990) and we added the Stokes I spot maps (Fig. 5) only for comparison purposes. The new observation generally confirms the paucity of 1667-MHz emission in the eastern side of the well pronounced 1612-MHz shell. The extent of 1667-MHz emission in the western side is the same as that of 1612-MHz shell, which indicates that the two masers operate at similar distances from the central star.

The locations and velocities of the Stokes I maser components at both frequencies obtained from the MERLIN observations are used to refine the shell parameters: stellar position, expansion and stellar velocities, outer, r_o and inner, r_i shell radius. The standard thin-shell model (Reid et al. 1977) was fitted to the Stokes I spots (Fig. 6) using a weighted least-squares algorithm. Parameters for the best fitting model are listed in Table 1. These are consistent with those reported by Bowers & Johnston (1990).

Assuming a spherical thin shell model with isotropic emission, the measurement of the 1612-MHz emission extent to the 3σ level integrated over the velocity range from −56.0 to −54.2 km s^{-1} reveals an OH shell radius of 1343±30 mas, which agrees with the estimate of the standard model (Table 1). The assumption of a spherical thin shell with isotropic emission allows us to consider this radius as the angular size of the shell. For non-isotropic emission, the angular size would be overestimated by ⩽10%. An increase of shell thickness and maser saturation leads to higher biases (van Langevelde & Spaans 1993). Combining the shell radius with the phase lag provided by the NRT observations, we obtain a distance of 3.87±0.28 kpc for OH127.

3.5 Spatial structure of the polarized emission

The polarization data obtained with MERLIN are analyzed using the standard methods (e.g Szymczak et al. 1998; Bains et al. 2003). Tables 3 and 4 list the parameters of the polarized components at both frequencies. Only the components
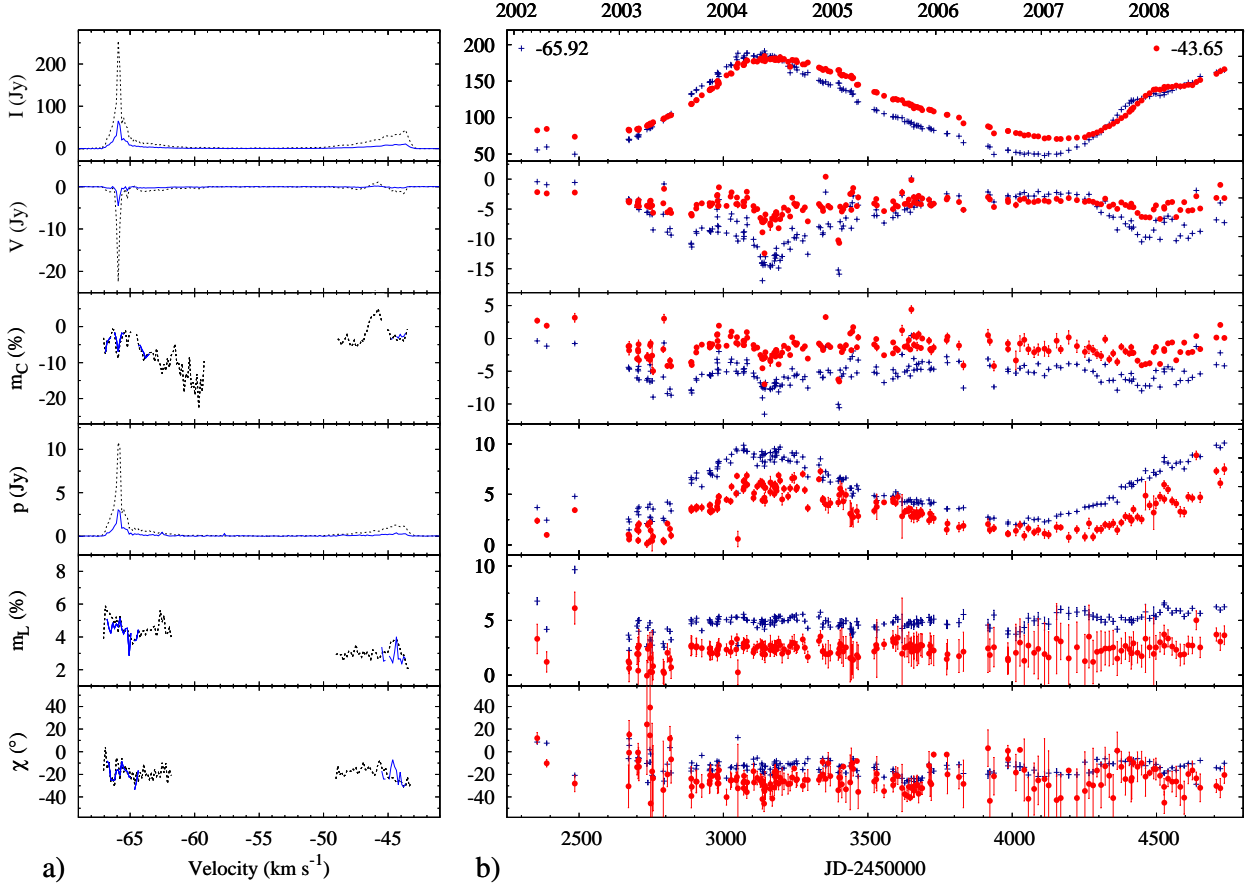
Figure 3. Polarization spectra of OH127 at 1612 MHz. (**a**) The dashed and solid lines are the average spectra for MJD ranges 3072−3203 (27 observations) and 4013−4168 (9 observations) near the maximum and minimum of the light curve, respectively. The Stokes I, V, degree of circular polarization, $m_{\rm C}$, linearly polarized flux density, p, degree of linear polarization, $m_{\rm L}$, and polarization position angle, χ, are shown from top to bottom. (**b**) Time-series of the polarimetric parameters for the extreme blue- ($-65.92\,{\rm km\,s^{-1}}$) and red-shifted ($-43.65\,{\rm km\,s^{-1}}$) emission peaks. For the Stokes I, V and p the left- and right-hand ordinates give the flux density scales for the extreme blue- and red-shifted peaks, respectively. Error bars are shown only for the red-shifted emission peak for sake **of** clarity but those for the blue-shifted emission peak are similar. For the Stokes I values the error bars are generally smaller than or of comparable size to the symbols.

with V and p brightness higher than $\sim$100 mJy beam^{-1} are listed. These make up about 10 and 7% of all Stokes I components at 1612 and 1667 MHz respectively.

The spatial distribution of the 1612-MHz polarized components is shown in Fig. 7. The origin of the maps is the position of the central star as derived from the standard model (Sect. 3.4). All of the 28 detected components have velocities larger than $0.65-0.70V_{\rm e}$ with respect to the stellar velocity and their typical Stokes V flux is $0.1-0.2$ Jy beam^{-1}. There is a strong excess of $-V$ components (20/28). The blue-shifted components are much closer to the projected position of the central star than the red-shifted components. The degree of circular polarization ranges from 5 to 38% which is a factor of 2 higher than that observed in the NRT spectra implying depolarization in the NRT beam. Difference in the spectral resolution by a factor of 1.5 between both instruments also plays a role. There are only a few components with elliptical polarization. The linearly polarized emission, generally weaker than 0.5 Jy beam^{-1} is detected from the blue-shifted part of the

spectrum. The components with $m_{\rm L} \leqslant 9\%$ appear in a cluster of size $\sim$400 mas located $\sim$200 mas west of the stellar position. The polarization angles range from -37 to $40°$ with a mean flux-weighted value of $-4°\!\!.6\pm12°\!\!.4$ that is consistent with the NRT results (Sect. 3.3).

The polarized 1667-MHz components are seen at the red-shifted velocities. The circularly polarized components of flux lower than 0.3 Jy beam^{-1} and $|m_{\rm C}| \leqslant 25\%$ are clustered near the stellar position (Fig. 8). All of them appear as LHC components which is consistent with the NRT results. The linearly polarized components show a similar location as the circularly polarized emission. The mean value of $m_{\rm L}=23.6\pm5.3\%$ is a factor 5 higher than that for the 1612-MHz emission. The mean flux-weighted polarization angle is $-9°\!\!.5\pm11°\!\!.5$. This agrees well with that at 1612 MHz and implies the same projected direction of magnetic fields in the regions of both OH masers.

While the degrees of circular polarization at 1612 and 1667 MHz are similar, the degrees of linear polarization at 1667 MHz are much higher than at 1612 MHz. This can im-
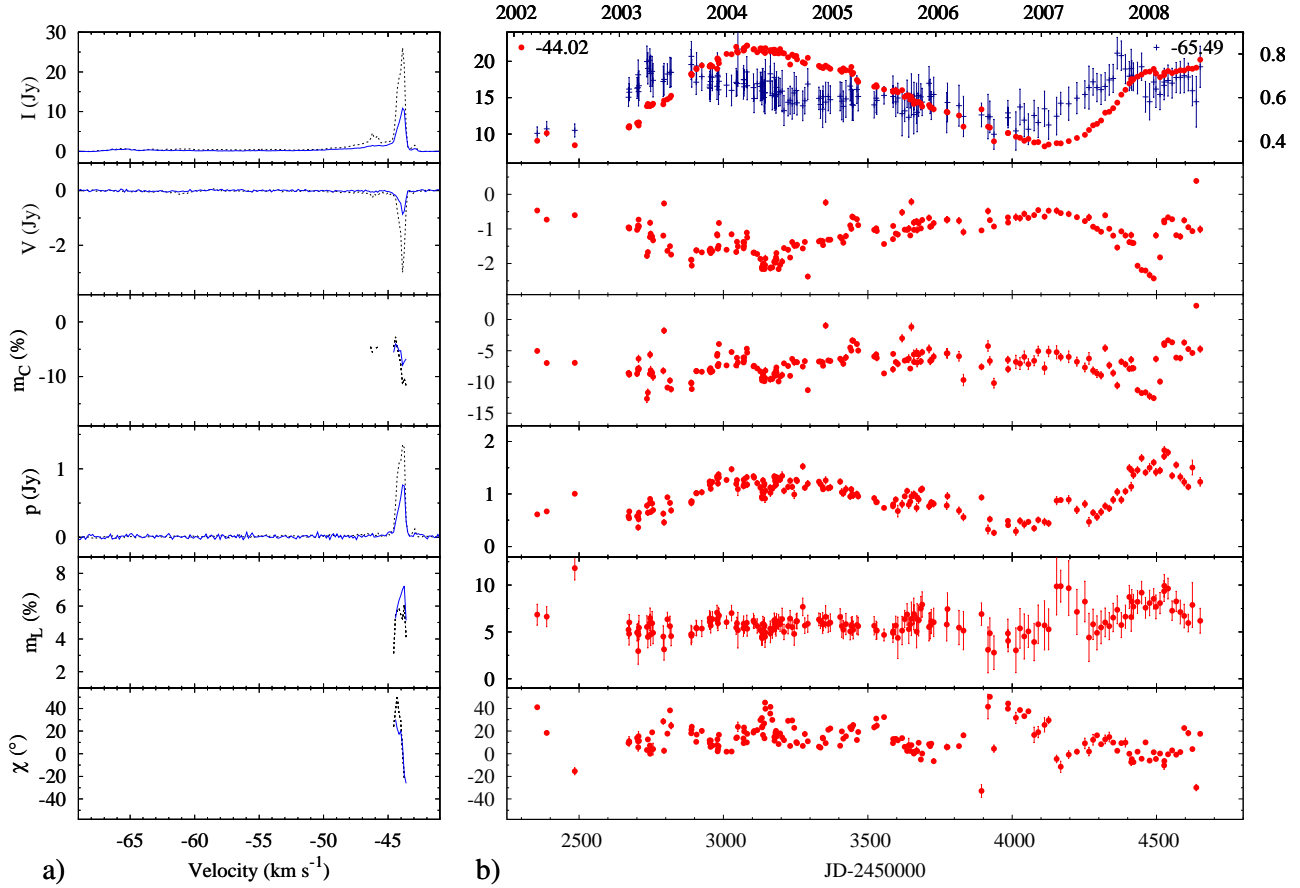
Figure 4. Same as in Fig.3 but for 1667-MHz line and with two exceptions: the average spectra are for MJD ranges 3081−3210 (27 observations) and 4042−4224 (9 observations) near the maximum and minimum of the light curve, respectively and that the time-series of all polarimetric parameters are shown for the extreme red-shifted (−44.02 km s^{-1}) emission peak, while the Stokes I flux density only is shown for the extreme blue-shifted (−65.49 km s^{-1}) emission peak.

ply that the linear polarization at 1612 MHz is suppressed or depolarized in the regions of strong amplification of this line (Elitzur 1996).

3.5.1 Magnetic field strength

Two groups of spatially coincident ($<0\rlap{.}''1$) RHC and LHC features at RA(J2000) = $01^{\rm h}33^{\rm m}51\rlap{.}^{\rm s}2247$, Dec(J2000) = $62°26'53\rlap{.}''311$ appear in 8 contiguous channels. These are marked by z in Table 3. The features are clearly asymmetric but can be easily fitted with two slightly shifted Gaussian components (Fig.9). The strongest component near −65.18 km s^{-1} shows a 0.142±0.045 km s^{-1} difference in the peak velocities between the RHC and LHC emissions. If one can interpret this difference as a Zeeman effect, then the magnetic field strength is −0.60±0.19 mG assuming an average splitting coefficient of the σ components (Davies 1974). Here, the minus sign indicates that the direction of the field is towards the Earth. No linearly polarized emission is detected at this position.

3.6 Emission from the near and far caps

The 1612-MHz emission in the velocity ranges from −66.8 to −66.0 km s^{-1} ($b_{\rm cap}$) and from −43.6 to −42.8 km s^{-1} ($r_{\rm cap}$) is unresolved or barely resolved with the MERLIN beam. The lower limits to the brightness temperature ($T_{\rm b}$) for $b_{\rm cap}$ and $r_{\rm cap}$ regions are $0.7−3.1×10^7$ and $3.3−6.3×10^7$ K, respectively. $T_{\rm b}$ of the emission from $b_{\rm cap}$ is a factor of $2−7$ higher than that of $r_{\rm cap}$, while the angular size is by $18−23\%$ lower. Both extreme regions coincide within 70 mas supporting the standard model of spherically symmetric shell. The emission from the near cap may contain a component from the amplified stellar image (Norris et al. 1984; van Langevelde & Spaans 1993; van Langevelde et al. 2000). We failed to verify this hypothesis due to the insufficient angular resolution of our data and the poorly known optical position of the underlying star.

4 DISCUSSION

4.1 Revised properties of OH127

The present observations allow us to refine the basic stellar parameters of OH127. Whitelock, Feast & Catchpole (1991)
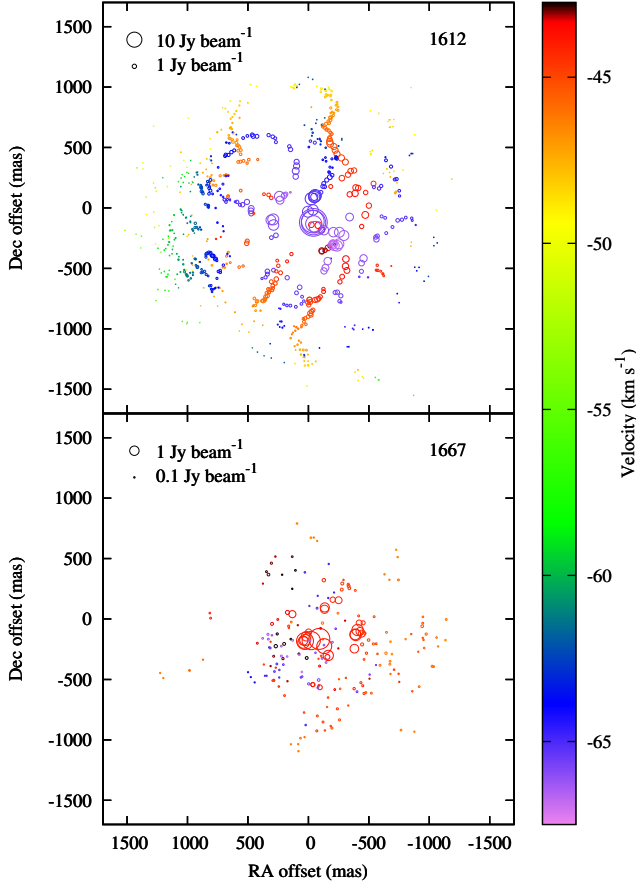
Figure 5. Stokes *I* maps of the 1612- and 1667-MHz maser spots of OH127. The symbol sizes are proportional to the logarithm of the brightness. The velocity scale is coded in colour.
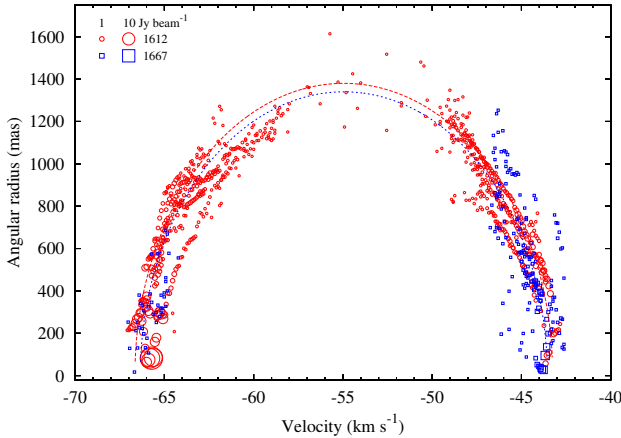

Figure 6. Angular distance of the maser emission spots from the estimated stellar position of OH127 versus their radial velocity. The symbol sizes are proportional to the logarithm of the brightness. The least-squares fits of the thin shell model to the data are used to estimate the shell parameters as listed in Table 1. The red-dashed and blue-dotted curves show the outer radii fitted to the maser distribution at 1612 and 1667 MHz, respectively.
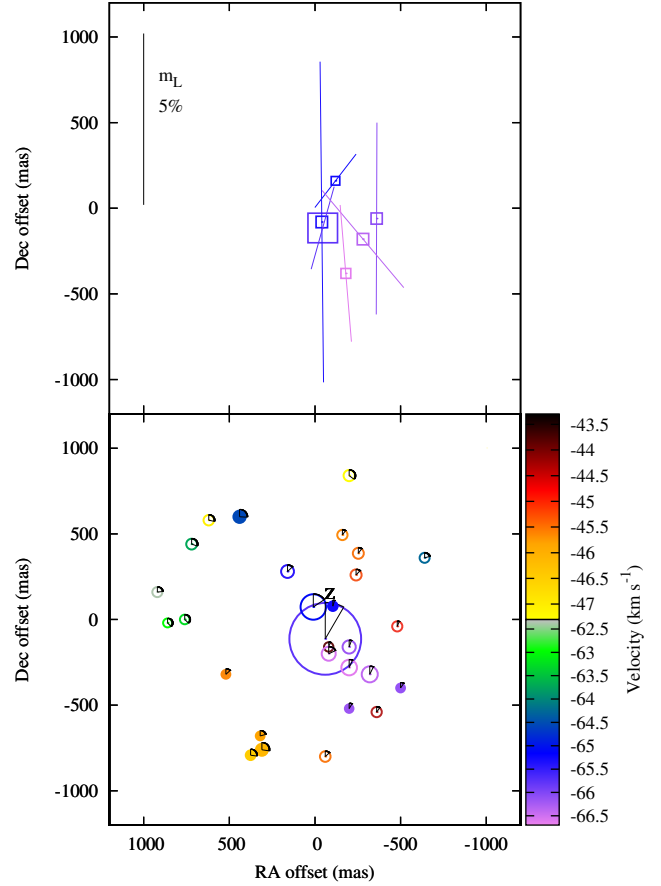

Figure 7. Distribution of the 1612-MHz maser polarized components of OH127. Velocities are coded by colours as shown in the bottom right wedge. *Upper panel*: linearly polarized components. The size of squares is proportional to the logarithm of the *p* flux density and the length of polarization vectors is proportional to the degree of linear polarization, m_L. *Lower panel*: circularly polarized components. The size of the circles is proportional to the logarithm of the Stokes *V* flux density. Empty and solid circles indicate negative and positive values of the Stokes *V*, respectively. The size of sectors is proportional to the degree of circular polarization.

derived a period-luminosity, $P - L_\star$ relation for OH/IR stars with pulsation periods of $1000-2000$ days. Using their eq. 2, one would predict that the luminosity of OH127 is $2.68^{+1.81}_{-1.08} \times 10^4 L_\odot$. The uncertainty is rather large but this value is close to $1.5 \times 10^4 L_\odot$, which is the value adopted by De Beck et al. (2010) scaled to our distance estimate. Kemper et al. (2002) obtained the best fit of the spectral energy distribution (SED) of OH127 to the observations at the distance of 1.8 kpc for the assumed luminosity $0.63 \times 10^4 L_\odot$ which translates to $2.9 \times 10^4 L_\odot$ for our distance estimate (Tab. 1). Thus, the stellar luminosity of OH127 is below the AGB-limit of $5.5 \times 10^4 L_\odot$ (Wood et al. 1983) but it is very luminous compared to a typical AGB star.

OH127 emits virtually all its radiation at infrared wavelengths and the mass-loss rate, $\dot{M}$, obtained from modelling of the spectral energy distribution (SED) is $1.5-2.8 \times 10^{-4} M_\odot \, \mathrm{yr}^{-1}$ (Justtanont & Tielens 1992; Kem-
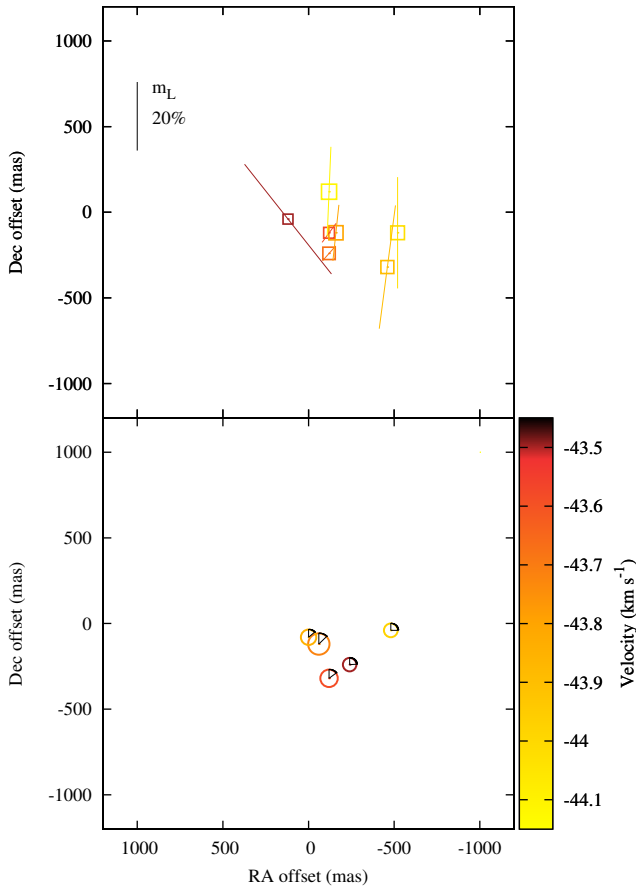
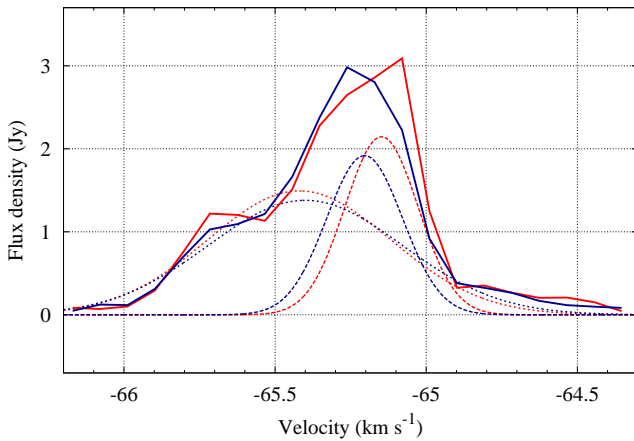**Figure 8.** Same as Fig. 7 but for the 1667-MHz emission.

Figure 9. MERLIN 1612-MHz spectra of the left (red solid line) and right (blue solid line) circular polarizations of maser features of close spatial coincidence. The dashed lines show the Gaussian curves fitted to the data. The strongest component near $-65.18\,\mathrm{km\,s^{-1}}$ exhibits a velocity shift between the left (red dashed line) and right (blue dashed line) circular polarizations, which is a signature of Zeeman splitting.

per et al. 2002) when scaled to our distance estimate and for an assumed dust to gas ratio of 0.01. The observations and modelling of multiple low- and high$-J$ CO lines (up to J = 7$-$6) by De Beck et al. (2010) give $\dot{M} = 3.4{\times}10^{-5}\mathrm{M_{\odot}\,yr^{-1}}$ for the distance of 3.87 kpc. The mass-loss rate calculated from an empirical formula based on the photo-dissociation model (Netzer & Knapp 1987) is $7.1{\times}10^{-5}\mathrm{M_{\odot}\,yr^{-1}}$. This value is only a factor of two higher than that obtained with CO observations (De Beck et al. 2010) and is typical for OH/IR stars. This indicates that the $\dot{M}$ estimates from the SED modelling are an order of magnitude higher than those from CO and OH data, likely due to the poorly constrained dust to gas ratio (Justtanont & Tielens 1992).

4.2   Magnetic field

The strength of the magnetic field tentatively detected in OH127 is comparable in magnitude with that estimated for other stellar OH maser sources (Szymczak et al. 1998; Bains et al. 2003; Amiri et al. (2010); Etoka & Diamond 2010). However, it is an order of magnitude higher than that measured from single dish high resolution spectra of several OH/IR objects (Zell & Fix 1991). This discrepancy is likely due to spatial blending of individual maser clumps in the envelopes and is confirmed for OH127: our NRT 1612-MHz spectra in the velocity range of -66.6 to $-64.5\,\mathrm{km\,s^{-1}}$ contain features with $m_C \leqslant 5\%$ while the MERLIN maps show highly (up to 38%) polarized components (Tab. 3).

The presence of magnetic field in the outer envelope of OH127 is implied by the net polarization observed in both OH transitions. Specifically, the source shows a strong excess of LHC emission well seen in the NRT spectra and MER-LIN maps (Figs. 3 $-$ 8). Enhancing one sense of circular polarization and inhibiting the other can be explained by the overlap of different Zeeman components due to a velocity gradient within the medium (Deguchi & Watson 1986) or matching the gradients of the magnetic field and velocity (Cook 1966). The latter mechanism may be less probable in a thin circumstellar shell. A simple model of dipole magnetic field with an adapted Cook's mechanism was successful in explaining the spatial segregation of the 1612-MHz spots dominated by the two senses of circular polarization in the supergiant star VX Sgr (Zell & Fix 1996). It is quite possible that Cook's mechanism could also partly explain the distribution of the 1612-MHz maser polarized components of OH127 (see Fig. 7) by adopting a scenario inspired from Zell & Fix's Fig. 4 but with dipole field lines stretched in the radial direction and a different inclination of the dipole axis to the line of sight. At a distance of 5350 au from the star a radial magnetic field or a field with open lines can occur. In the first case the outflow velocity gradient can combine with the Zeeman pair to produce a coherence length of maser amplification longer for LHC component than for RHC component at the near and far sides of the envelope, i.e. the blue- and red-shifted parts of the spectrum are dominated by LHC emission. If the field with open lines or of interstellar origin is oriented towards the observer, as shown by our observations, then the masers from the near and far sides of the envelope will be dominated by LHC and RHC emission, respectively. This scenario is not fully consistent with our data where the red wing shows positive and nega-

tive values of m_C at 1612 MHz and only negative values at 1667 MHz.

OH127 at 1612 MHz shows very small differences in the polarization angles at the near and far sides of the shell, suggesting a regular configuration of the magnetic field. Such a phenomenon was observed in other OH/IR objects and two explanations are proposed in Wolak et al. (2012): (1) the field is of stellar origin and the same orientation of the field is carried away by the wind flowing towards the near and back sides of the shell, (2) the field is of interstellar origin and can be amplified and/or distorted by the stellar wind.

In the first case the field of 0.6 mG strength of solar type ($B \sim r^{-2}$) gives a surface field strength of $\sim$1kG for the assumed star radius of $859R_\odot$ (De Beck et al. 2010), which is $\leqslant 10^3$ times stronger than the average magnetic field ($\sim$few G) for an AGB star (Kemball & Diamond 1991). In the second case, if the magnetic field pressure equals the gas kinetic pressure, then $B^2/8\pi \sim \rho V_e^2$, where ρ is the gas density in g cm^{-3}. Since $\rho = \dot{M}/4\pi r^2 V_e$ for a free radial expansion then $B(G) \sim (2\dot{M}V_e)^{0.5}/r$. With $\dot{M}$ in units of $10^{-5}M_\odot$ yr^{-1}, V_e in units of 10 km s^{-1} and the distance to the star, r in au we obtain

$$B(G) = 2.4 \times (2\dot{M}V_e)^{0.5}/r. \qquad (1)$$

For $\dot{M} = 3.4$ (De Beck et al. 2010), $V_e = 1.12$, r=5350 au (Table 1) this equation yields a B field strength of 0.9 mG, which is close to our value of 0.6 mG. This means that in our measured OH maser region there is nearly equilibrium between the magnetic and kinematic pressure. Eq. 1 may not be true close to the star where a solar ($\sim r^{-2}$) or dipole ($\sim r^{-3}$) type field may exist. On the other hand, the magnetic field measurements from maser observations indicate that the field strength follows the relation $B \sim n^{0.5}$ over an enormous range of the number density, n, (Vlemmings 2012). This empirical relation predicts a number density of molecular hydrogen of 1×10^5 cm^{-3} for a 0.6 mG field. For the kinematic model (Sun & Kwok 1987) such a density is sufficient to sustain the 1612-MHz maser operation when $\dot{M} > 5 \times 10^{-5}$ and $> 1 \times 10^{-5}M_\odot$ yr^{-1} for relative abundances of OH molecule higher than 2×10^{-4} and 5×10^{-4}, respectively. These mass-loss rate values are consistent with those recently obtained with the CO observations and modelling (De Beck et al. 2010 and Sect. 4.1).

We note that a magnetic field of 0.6 mG is two orders of magnitude larger than the average interstellar magnetic field (Troland & Heiles 1986). This suggests that the magnetic field in the OH regions could be compressed or amplified by a factor of $\sim$100 (Soker 2002). A model of field compression by Gérard (1985) predicts an amplification factor of up to 10. Another possibility is local enhancements of the magnetic field related to the stellar spots or convective cells which might produce the magnetic clouds similarly as in the solar wind (Soker 2006).

4.3 Saturation level

Our observations show that the lower limit to the brightness temperature of the strongest 1612-MHz emission is up to 6×10^7 K (Sect. 3.6). VLBI observations at a phase of 0.67 detected only the extreme blue-shifted emission near

-66.0 km s^{-1}, which was unresolved with $\sim$100 mas resolution, while the extreme red-shifted emission was resolved out (Norris et al. 1984). T_b for the unresolved emission was estimated at 5×10^9 K. Our MERLIN data were obtained at phase 0.44, so it is likely that the flux density level was similar to that observed with the VLBI. Using the VLBI estimates of size and brightness temperature for the extreme blue-shifted emission and the distance and shell radius given in Table 1 we estimated that the maser beaming solid angle, Ω, is 0.016 sr. This is close to the canonical value (Goldreich & Keeley 1972). From our comparison of the angular sizes of the two extreme maser regions (Sect. 3.6) we get $0.022-0.024$ sr for the beaming solid angle of the red-shifted emission. In the standard maser theory (Goldreich, Keeley & Kwan 1973) the 1612 MHz maser stimulated emission rate can be approximated (Amiri et al. 2010)) by

$$R = 1.3 \times 10^{-2} \left(\frac{T_b}{10^{10}\text{K}}\right) \left(\frac{\Omega}{10^{-2}\text{sr}}\right) \text{s}^{-1} \qquad (2)$$

This implies $R = 0.011$ s^{-1} and $0.008-0.002$ s^{-1} for the blue- and red-shifted emission regions, respectively. We notice that the first value is consistent with R predicted for interstellar OH masers (Goldreich et al. 1973). The radiative and collisional decay rate for the 1612 MHz is not observationally constrained but its upper limit can be estimated (Elitzur 1992) with the following equation

$$\Gamma < 2.7 \times 10^{-2} \left(\frac{T_b}{10^{10}\text{K}}\right) \left(\frac{\Omega}{10^{-2}\text{sr}}\right) \text{s}^{-1} \qquad (3)$$

With the above estimated values of T_b and Ω for the blue-shifted emission $\Gamma < 1.5 \times 10^{-3}$ s^{-1} which implies $R/\Gamma >7$, i.e. the maser in OH127 is weakly saturated. This result appears to be consistent with previous observations showing a fixed relation between the OH and infrared emissions (Harvey 1974). The lack of relatively large random variations in the OH maser fluxes of OH127 also suggests that the maser emission is saturated.

5 SUMMARY AND CONCLUSIONS

Full polarization monitoring of 1612- and 1667-MHz OH maser lines over a period of 6.5 years and one epoch polarimetric map of OH127 led to the following new results:

(1) The OH maser fluxes show large $(0.8-1.4$ mag) amplitude variations with period of $\sim$1600 days. The ratios of the integrated flux at 1612 and 1667 MHz lines of 5.4 and 9.9 at the minimum and maximum, respectively indicate a partial suppression of the 1667 MHz emission.

(2) The comparison of the light-travel diameter of the 1612-MHz maser shell obtained using the NRT with the angular diameter determined from MERLIN maps yields a distance of 3.87±0.28 kpc.

(3) The fluxes of polarized emission follow the variations of the total flux, whereas the degrees of circular and linear polarization are constant within measurement accuracy.

(4) The tentative detection of a Zeeman pair at 1612 MHz implies a magnetic field strength of -0.6 mG at a distance of $\sim$5400 au. The strong alignment of polarization position angles at both the near and far sides of the shell and the presence of a net polarization suggest a regular magnetic field.

(5) The stellar luminosity of OH127 is slightly below

the AGB limit and the mass loss rate is typical for an AGB star.

(6) The measured sizes of the compact emissions from the near and far sides of the shell and the lower limits to the brightness temperature imply weakly saturated emission.

ACKNOWLEDGMENTS

REFERENCES

Amiri N., Vlemmings W., van Langevelde H.J., 2010, A&A, 509, 26

Bains I., Gledhill T.M., Yates J.A., Richards A.M.S. 2003, MNRAS, 338, 287

Baud B., Habing H.J., Matthews H.E., Winnberg A. 1981, A&A, 95, 156

Booth R.J., Kus A.J., Norris R.P., Porter N.D. 1981, Nat, 290, 382

Bowers P.F., Johnston K.J. 1990, ApJ, 354, 676

Bowers P.F., Johnston K.J., Spencer J.H. 1983, ApJ, 274, 733

Chapman J.M., Cohen. R.J. 1986, MNRAS, 220, 513

Chen P.S., Szczerba R., Kwok S., Volk K. 2001, A&A, 368, 1006

Cohen R.J. 1989, RPPh, 52, 881

Cook A.H. 1996, Nat, 211, 503

David P., Etoka S., Le Squeren A. M. 1996, A&AS, 115, 387

Davis R.D. 1974, in Kerr F. J., Simonson S. C., eds, IAU Symp. 60, Galactic Radio Astronomy. Reidel, Dordrecht, p. 275

De Beck E., Decin L., de Koter A., Justtanont K., Verhoelst T., Kemper F., Menten, K.M., 2010, A&A, 523, A18

Deguchi S., Watson W.D., 1986, ApJ, 300, L15

Diamond P.J, Garrington S.T, Gunn A.G, Leahy J.P., Mc-Donald A., Muxlow T.W.B., Richards A.M.S., Thomasson, P., 2003, MERLIN User Guide,
http://www.merlin.ac.uk/user_guide/

Diamond P.J., Norris R.P., Booth R.S., 1985, MNRAS, 216, 1

Elitzur M., 1992, in Astronomical Masers, Kluwer Publishers, 59

Elitzur M., 1996, ApJ, 457, 415

Elitzur M., Goldreich P., Scoville N., 1976, ApJ, 205, 384

Etoka S., Diamond P.J., 2010, MNRAS, 406, 2218

Gérard E., 1985, A&A, 146, 1

Goldreich P., Keeley D.A., 1972, ApJ, 174, 517

Goldreich P., Keeley D., Kwan J.Y., 1973, ApJ, 182, 55

Goldreich P., Scoville N., 1976, ApJ, 205, 144

Gray M.D., Field D., 1995, A&A, 298, 243

Groenewegen M.A.T., Sloan G.C., Soszynski I., Petersen, E.A., 2009, A&A, 506, 1277

Habing H.J., 1996, A&AR, 7, 97

Harvey, P.M., Bechis, K.P., Wilson, W.J.; Ball, J.A., 1974, ApJ, 27, 331

Herman J., Habing, H.J., 1985, A&AS, 59, 523

Justtanont K., Tielens A.G.G.M., 1992, ApJ, 389, 400

Kemball A.J., Diamond P.J., 1997, ApJ, 481, L111

Kemper F., de Koter A., Waters L.B.F.M., Bouwman J., Tielens A.G.G.M., 2002, A&A, 384, 585

Kerr F.J., Bowers P.F. 1974, A&A, 36, 225

Lebzelter T., 2011, AN, 332, 140

Lépine J.R.D., Ortiz R. Epchtein, N., 1995, A&A, 299, 453

Likkel L., 1989, ApJ, 344, 350

Netzer N., Knapp G.R., 1987, ApJ, 323, 734

Norris R.P., Booth R.S., Diamond P.J., Nyman L.-A., Graham D.A., Matveenko L.I., 1984, MNRAS, 208, 435

Norris R.P., Diamond P.J., Booth, R.S., 1982, Nature, 299, 131

Reid M.J., Muhleman D.O., Moran J.M., Johnston K.J., Schwartz P.R., 1977, ApJ, 214, 60

Soker N., 2002, MNRAS, 336, 826

Soker N., 2006, PASP, 118, 260

Sun J., Kwok S., 1987, A&A, 185, 258

Szymczak M., Cohen R.J., Richards A.M.S., 1998, MNRAS, 297, 1151

Szymczak M., Cohen R.J., Richards A.M.S., 2001, A&A, 371, 1012

Szymczak M., Gérard E., 2004, A&A, 423, 209

Troland T.H., Heiles C., 1986, ApJ, 301, 339

van der Veen W.E.C.J., Habing H.J., 1988, A&A, 194, 125

van Driel, W., Pezzani, J., Gérard, E. 1996, in High sensitivity radio astronomy, ed. N. Jackson & R. J. Davis, Cambridge Univ.Press, 229

van Langevelde H.J., Spaans M., 1993, MNRAS, 264, 597

van Langevelde H.J., van der Heiden R., van Schooneveld C., 1990, A&A, 239, 193

van Langevelde H. J., Vlemmings W., Diamond P. J., Baudry A., Beasley A. J., 2000, A&A, 357, 945

Vassiliadis E., Wood P.R., 1993, ApJ, 413, 641

Vlemmings W.H.T., 2012, in Cosmic Masers- from OH to Ho, IAU Symposium 287, 31

Whitelock P., Feast M., Catchpole R., 1991, MNRAS, 248, 276

Wolak P., Szymczak M., Gérard, E., 2012, A&A, 537, A5

Wood P.R., Bessell M.S., Fox M.W., 1983, ApJ, 272, 99

Zell P.J., Fix J.D., 1991, ApJ, 369, 506

Zell P.J., Fix J.D., 1996, AJ, 112, 252

Table 3. Highly circularly polarized components in OH127.8+0.0. The columns are as follows: (1) RA and DEC relative to the shell centre (Table 1); (2) the peak Stokes I flux density, together with the rms (1σ); (3) the peak Stokes V flux density, together with the rms (1σ); (4) the degree of circular polarization, together with the rms (1σ); (5) the peak p flux density, together with the rms (1σ); (6) the degree of linear polarization, together with the rms (1σ); (7) the LSR velocity of the component; (8) Zeeman pair.

RA	Dec	$I(\sigma_I)$	$V(\sigma_V)$	$m_{\mathrm{C}}(\sigma_{m_{\mathrm{C}}})$	$p(\sigma_p)$	$m_{\mathrm{L}}(\sigma_{m_{\mathrm{L}}})$	v_{LSR}	notes
(mas)		(mJy b^{-1})		(%)	(mJy b^{-1})	(%)	(km s^{-1})	
(1)		(2)	(3)	(4)	(5)	(6)	(7)	(8)
				1612 MHz				
−200	−240	3145(23)	−213(21)	−6.8(0.7)			−66.63	
−80	−160	1016(21)	−183(18)	−18.0(2.1)			−66.53	
−320	−280	3030(19)	−221(18)	−7.3(0.6)	63(12)	2.1(0.4)	−66.40	
−200	−120	3201(24)	−168(18)	−5.2(0.6)	92(12)	2.9(0.4)	−66.17	
−60	−70	22260(49)	−1870(27)	−8.4(0.2)	617(13)	2.8(0.1)	−65.76	
160	320	1250(24)	−160(20)	−12.8(1.8)			−65.44	
10	70	2651(20)	−413(18)	−15.6(0.6)			−65.08	z
−640	400	534(20)	−111(16)	−20.8(3.8)			−64.26	
720	480	413(18)	−125(16)	−30.2(5.2)			−63.72	
860	20	244(18)	−93(16)	−38.1(9.4)			−62.95	
920	200	482(18)	−112(16)	−23.2(4.2)			−62.36	
760	40	279(19)	−104(16)	−37.2(8.3)			−62.27	
−200	−480	1463(24)	121(18)	8.3(1.4)			−66.17	
−500	−360	1345(25)	126(18)	9.4(1.5)			−66.13	
−100	80	2808(21)	139(18)	4.9(0.7)			−65.26	z
440	640	724(20)	188(16)	26.0(3.0)			−64.54	
−200	880	369(20)	−131(16)	−35.5(6.3)			−47.28	
620	620	420(19)	−119(18)	−28.3(5.6)			−46.96	
−250	430	1179(20)	−116(16)	−9.8(1.5)			−44.92	
−60	−760	912(20)	−122(18)	−13.4(2.3)			−44.70	
−240	300	1073(20)	−130(17)	−12.1(1.8)			−44.24	
−480	0.0	1754(20)	−115(18)	−6.5(1.1)			−43.83	
−360	−500	1158(18)	−116(17)	−10.0(1.6)			−43.60	
−80	−120	1721(19)	−102(18)	−5.9(1.1)			−43.47	
380	−750	520(19)	141(17)	27.1(4.2)			−46.15	
310	−720	663(19)	183(17)	27.6(3.3)			−45.69	
320	−640	600(19)	124(16)	20.7(3.3)			−45.28	
520	−280	942(20)	125(16)	13.3(2.0)			−44.92	
				1667 MHz				
−240	200	715(19)	−173(23)	−24.2(3.8)			−44.00	
−480	0	711(21)	−178(24)	−25.0(4.1)	93(16)	13.0(2.6)	−43.98	
0	−40	1490(20)	−209(22)	−14.0(1.7)	90(16)	6.0(1.5)	−43.85	
−60	−80	2695(24)	−326(23)	−12.1(1.0)	90(16)	3.3(0.6)	−43.72	
−120	−280	1684(23)	−247(22)	−14.7(1.5)			−43.58	

Table 4. Highly linearly polarized components in OH127.8+0.0. The columns are as follows: (1) RA and DEC relative to the shell centre (Table 1); (2) the peak Stokes I flux density together with the rms (1σ); (3) the p peak flux density together with the rms (1σ); (4) the degree of linear polarization together with the rms (1σ); (5) the polarization position angle together with the rms (1σ); (6) the peak Stokes V flux density together with the rms (1σ); (7) the degree of circular polarization together with the rms (1σ); (8) the LSR velocity of the component.

RA	Dec	$I(\sigma_I)$	$p(\sigma_p)$	$m_L(\sigma_{m_L})$	$\chi(\sigma_\chi)$	$V(\sigma_V)$	$m_C(\sigma_{m_C})$	v_{LSR}
(mas)		(mJy b^{-1})		(%)	(°)	(mJy b^{-1})	(%)	(km s^{-1})
(1)		(2)	(3)	(4)	(5)	(6)	(7)	(8)
				1612 MHz				
−180	−340	2733(21)	108(12)	4.0(0.5)	4.7(1.9)			−66.63
−280	−140	3701(21)	136(12)	3.7(0.3)	40.0(1.7)	−128(18)	−1.7(0.25)	−66.35
−360	−20	2354(26)	132(12)	5.6(0.6)	−0.2(5.1)			−66.08
−45	−75	19747(42)	505(13)	2.5(0.9)	−15.5(1.0)	−11013(27)	−7.0(0.1)	−65.76
−40	−40	1461(26)	137(11)	9.4(0.9)	0.6(1.7)			−65.35
−120	200	4396(19)	86(11)	2.0(0.3)	−37.6(2.2)	252(18)	5.7(0.4)	−65.26
				1667 MHz				
−120	160	773(22)	203(16)	26.3(2.8)	−2.4(1.4)			−44.11
−520	−80	545(20)	177(16)	32.5(4.1)	0.1(1.5)	−100(23)	−18.3(4.9)	−44.02
−460	−280	449(23)	163(15)	36.3(5.2)	−7.5(1.5)			−43.89
−160	−80	1127(25)	185(16)	16.4(1.8)	−6.1(1.5)	96(23)	8.5(2.2)	−43.80
−120	−200	2641(26)	153(16)	5.8(0.7)	−41.7(1.6)	−189(22)	−7.1(0.9)	−43.67
−120	−80	1810(23)	125(16)	6.9(1.0)	−36.2(1.8)	−165(22)	−9.1(1.3)	−43.58
120	0	268(18)	110(15)	41.0(8.3)	38.3(2.8)			−43.50